


Bifurcations to turbulence in transitional channel flowMasaki Shimizu ^{*}*Graduate School of Engineering Science, Osaka University, Toyonaka, 560-0043, Japan*Paul Manneville [†]*Hydrodynamics Laboratory, CNRS-UMR 7646, École Polytechnique, Palaiseau, 91128, France*

(Received 20 August 2018; published 22 November 2019)

In wall-bounded parallel flows, sustained turbulence can occur even while laminar flow is still stable. Channel flow is one of such flows and displays spatiotemporal fluctuating patterns of localized turbulence along its way from and to featureless turbulence. By direct numerical simulation, we study the observed inconsistency between turbulence decay according to a two-dimensional directed-percolation (2D-DP) scenario and the presence of sustained oblique localized turbulent bands (LTBs) below the DP critical point. Above Reynolds number $Re_g \approx 700$, sustained LTBs are observed; most LTBs have the same orientation so that the spanwise symmetry of the LTB pattern is broken below $Re_2 \approx 1000$. The frequency of transversal splitting, by which an LTB generates another one with opposite obliqueness, so that turbulence spreading becomes intrinsically two dimensional, increases in the range $Re_g < Re < Re_2$. It reaches a critical rate at Re_2 , beyond which symmetry is restored. The 2D-DP behavior is retrieved only above Re_2 . A mean-field model is proposed which qualitatively accounts for the above symmetry-restoring bifurcation by considering interactions between space-averaged densities of LTBs propagating in either direction.

DOI: [10.1103/PhysRevFluids.4.113903](https://doi.org/10.1103/PhysRevFluids.4.113903)**I. INTRODUCTION**

The ways shear flows become turbulent markedly depend on the shape of their laminar velocity profiles and the occurrence of instability mechanisms of Kelvin-Helmholtz type affecting them. Inflectional profiles like in free shear layer, wakes, or jets become unstable at rather low values of the Reynolds number against such modes of inertial origin and then turn turbulent through a continuous cascade of successive instabilities [1], each step being in principle captured by weakly nonlinear perturbation theory, resulting in a *globally supercritical* transition to turbulence. By contrast, unidirectional flows controlled by the shear at solid walls do not display inflection points and are not prone to such instability modes. They may become unstable but only against more intricate and counterintuitive mechanisms involving viscous dissipation [1,2]. The so-produced Tollmien-Schlichting waves develop only at high Reynolds number, beyond a certain linear threshold Re_c (later denoted Re_{TS} for convenience). Pipe flow in tubes of circular and square sections or plane Couette flow between flat countertranslating plates remain linearly stable for all Re , $Re_c \rightarrow \infty$, whereas for channel flow (plane Poiseuille flow) $Re_c < \infty$ [3]. For such flows, the transition is *globally subcritical*. Physically infinitesimal perturbations are, however, not mathematically infinitesimal but only finite but small, and the possibility of a direct transition to turbulence, called *bypass*, is in practice observed at moderate values of Re due to the nonlinearity of the Navier-Stokes

^{*}shimizu@me.es.osaka-u.ac.jp[†]paul.manneville@ladhyx.polytechnique.fr

equations: At increasing Re , the flow can in principle be maintained steady and laminar up to $Re_c \leq \infty$, but the introduction of finite perturbations with particular shapes and amplitudes may force it to become unsteady. There is therefore a full range of Reynolds numbers, called *transitional*, where the trivial laminar solution coexists with other nontrivial solutions. These solutions are usually chaotic and cannot be straightforwardly reached by standard perturbation analysis. A direct transition to turbulence is observed with strong hysteresis upon continuous up-and-down variation of Re , the flow jumping from the laminar solution branch to the nontrivial turbulent branch or back. Once in a state belonging to the nontrivial branch, the flow can be maintained turbulent down to a global stability threshold Re_g below which the only possible stable regime is laminar.

Subcriticality is often perceived as a problem to be studied within the theory of dynamical systems. Solutions to the Navier-Stokes equations are then searched under minimal flow unit (MFU) conditions [4] with periodic boundary conditions at short distances, focusing on coherent structures analyzed in the corresponding *phase space* perspective [5,6]. This approach was progressively generalized to deal with extended systems in one or two in-plane directions, and mostly concentrated on the existence and properties of isolated localized solutions at the edge of chaos; see, e.g., Ref. [7] for channel flow. On the other hand, when appreciated in *physical space*, provided that the system's geometry is wide enough, states along the nontrivial branch in general display a coexistence of domains alternately laminar and turbulent separated by fluctuating interfaces.

In a number of cases, beyond Re_g this laminar-turbulent coexistence happens in the form of a regular pattern. The iconic case is that of the turbulent spiral obtained in moderate-gap cylindrical Couette flow by Coles [8], and reobtained later by Andereck *et al.* [9], who introduced the term *featureless* to qualify the regime obtained at higher shearing rates when turbulence has apparently returned to statistical uniformity. In small-gap experiments, several helical branches were obtained [10]. Close to the featureless regime, laminar-turbulent patterning involved superpositions of such helices with opposite pitch while, plane Couette flow being understood as the zero-curvature limit of cylindrical Couette flow, helices were straightened into oblique bands found in a whole range of Re down to Re_g [10]. As Re increased, the amplitude of the turbulence modulation associated with these bands or helices was seen to decrease, and a threshold usually denoted as Re_t could be determined above which turbulence was featureless. The transition at Re_t seemed continuous, with a major role played by the intense noise arising from the chaotic dynamics in the turbulent regime [10,11]. Regular laminar-turbulent patterning with similar characteristics has been observed in a few other cases including stratified Ekman boundary layer [12], Couette-Poiseuille flow [13], or stratified plane Couette flow [14]. Experimental evidence for laminar-turbulent oblique patterning in channel flow was provided by Tsukahara's group [15] as a follow-up to their simulations in wide domains [16]. Another numerical approach using the oblique-elongated-but-narrow domain assumption [17] was developed in Ref. [18] to yield similar patterns at a much more limited numerical cost.

The location of the lower threshold Re_g is another problem that can be studied either by increasing Re from a germ or by decreasing Re from a pattern. In the first case, the study mostly relies on the capability to produce localized states and study their persistence. The first solid results were obtained in pipe flow (consult Ref. [19] for a general perspective and references back to Reynolds' seminal work) for which the relevant localized states are *puffs* and the threshold Re_g identified the value of Re when the probability of turbulence extinction due to their decay is overcome by the probability of their proliferation due to repeated splittings [20]. In planar flows, such as in planar boundary layers, plane Couette flow [21], Couette-Poiseuille flow [13], or channel flow [22], equivalent localized solutions appear as *turbulent spots* (see Ref. [23] for a recent study). The specific effect of spanwise extension on localization has been studied in small-aspect-ratio rectangular duct flow [24] and in annular Poiseuille flow [25]. In all cases, the location of Re_g is derived from statistical studies, with the difficulty that a wide range of initial conditions needs to be considered by varying their shapes, structures, and strengths. A value $Re_g \approx 1000$ was mentioned in Ref. [22] for channel flow and was also reported in other systems provided that the Reynolds number is based on an appropriate physically based estimate of the shear [26, Appendix]. The second approach, i.e., by decreasing Re , is also statistical but rather appeals to an early conjecture

by Pomeau [27], who put forward the analogy between turbulence onset and decay in extended systems and directed percolation (DP). This conjecture was based on the recognition that DP is a spatiotemporally intermittent process involving *active* (here turbulent) and *absorbing* (here laminar) states defined locally in physical space, and the probability of contamination of the latter by the former is the key factor. DP is the representative of a class of nonequilibrium phase transition with specific universal properties depending on the effective dimension D of the physical space in which the process develop [28]. Conceptually, the corresponding critical point Re_{DP} should have to be identified with Re_g and the long turbulent transients observed for $\text{Re} < \text{Re}_g$ as the decay of a percolation cluster below threshold.

Flows evolve physically in three-dimensional domains but confinement in the wall-normal direction reduces the dimension to an effective value $D = 1$ in tubes and flow configurations similarly constrained by lateral boundary conditions or $D = 2$ when the lateral boundaries are far enough when compared to the typical wall-normal distance. This is because the transitional range takes place at moderate Re so that viscosity is able to impose a strong coherence except along the unbounded directions, one in tubes or two along plates. To our knowledge, $1D$ -DP universality has not been checked directly in tubes up to now, but a numerical model suggests it might apply [29]. On the other hand, universality has been shown to hold quantitatively in a numerical model of plane shear flow defined in a narrow oblique domain [30,31] (a geometry introduced in Ref. [17]) and in a cylindrical Couette configuration with a small axial aspect ratio ensuring quasi- $1D$ confinement [31]. Similar findings have also been obtained in a model of two-dimensional shear flow without walls, called Kolmogorov flow, in an elongated domain that renders the dynamics effectively $1D$ [32]. As to $2D$ -DP universality, the corresponding critical behavior has been obtained with great precision in a numerical experiment on a low-order Galerkin approximation to Waleffe flow, which is a three-dimensional shear flow mimicking plane Couette flow but with stress-free boundary conditions [33]. Preliminary results on plane Couette flow proper, but in an under-resolved numerical context [34], suggest a similar conclusion. At last, agreement with $2D$ -DP universality has been obtained by Sano and Tamai [35] in a laboratory experiment on channel flow through a duct with a rectangular section and large spanwise aspect ratio. This finding has, however, to be reinterpreted in view of the discovery of sustained nontrivial solutions below Re_{DP} that could therefore not be the expected global stability threshold.

These solutions were first obtained in the form of a localized turbulent band (LTB) by triggering [36] and later upon looking for the global stability threshold by slowly decreasing Re and following the mutations in the laminar-turbulent patterning [37,38], by contrast with experiments in Ref. [35], where the decay from homogeneous turbulence was studied in a channel of limited length. They were later studied in more detail in Ref. [39], where sustainment mechanisms were scrutinized, and in Ref. [40], where their decay was considered in relation with the size of the numerical domain. Localized solutions with an analogous structure were also obtained in laboratory experiments [41,42].

Below we present our simulation results for channel flow in wide domains. An overview of the observed flow regimes is given in Sec. II, from LTBs around Re_g to the oblique pattern regime described in Refs. [15,16] and to featureless turbulence above Re_t . We next show in two steps how the contradiction between the observation of a $2D$ -DP scenario as reported in Ref. [35] can be reconciled with that of LTBs at lower Re . In Sec. III, we enter the details of how LTBs grow and split as Re increases and how spanwise symmetry is restored from the low- Re regime where LTBs move essentially in one direction [36–42]. A simple phenomenological model is developed to show that this bifurcation is controlled by the increasing rate of *transversal* splitting, thereby supporting the existence of a well-defined threshold. Above that threshold, the invasion of turbulence is genuinely $2D$ in the plane of the flow, in the form of a spatiotemporally intermittent network, where a DP-like behavior becomes relevant. The quantitative analysis of the turbulent fraction in Sec. IV will give evidence of a growth compatible with $2D$ -DP universality. Our findings are summarized in Sec. V, where we discuss in particular how processes specific to particular flow configurations may come and breach the appealing concept of universality expected on general grounds. Details on our

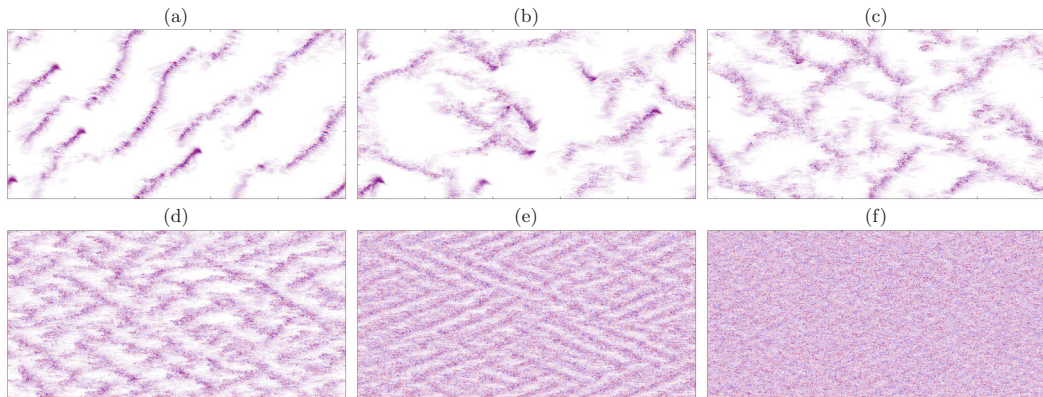


FIG. 1. (a) $Re = 850$ ($Re_b \approx 789$): one-sided LTB regime. (b) $Re = 1050$ ($Re_b \approx 947$): two-sided LTB regime. (c) $Re = 1200$ ($Re_b \approx 1012$): strongly intermittent loose continuous network of LTBs. (d) $Re = 1800$ ($Re_b \approx 1237$): weakly intermittent loose banded pattern. (e) $Re = 3000$ ($Re_b \approx 1604$): tight banded pattern. (f) $Re = 4000$ ($Re_b \approx 1843$): nearly featureless state. Flow direction is from the left to right. The wall-normal velocity field on the center plane ($y = 0$) is displayed. Domain size is 500×250 . See video in the Supplemental Material [43].

simulations and the filtering-thresholding methodology used to measure the turbulent fraction are presented in Appendixes A and B, respectively.

II. OVERVIEW OF THE TRANSITIONAL RANGE

Channel flow here is driven by a constant body force f . The Reynolds number is defined as $Re = fh^3/2\nu^2$, where h is the half-distance between two parallel walls and ν is the kinematic viscosity. All quantities below are written in units of the center-plane velocity of the corresponding laminar flow $U = fh^2/2\nu$ and h . For comparison with previous works, we also define $Re_b = \frac{3}{2}\langle U_m \rangle Re$, where $\langle U_m \rangle$ is the time average of the dimensionless bulk velocity U_m (“b” stands for “bulk” [18]). Most of the time, the computational domain size is 500×250 (streamwise \times spanwise) but we also consider 250×125 and 1000×500 to check for size effects. Simulations are performed for durations sufficient to obtain statistically significant results, typically up to 1.5×10^5 time units. See Appendix A for a detailed description of the flow system and the numerical procedures.

Snapshots of flow patterns for typical Reynolds numbers are displayed in Fig. 1. For $Re = 850$ and 1050 , Figs. 1(a) and 1(b), several localized turbulent bands (LTBs) are observed, propagating at an angle about 45° with the streamwise direction, each driven by a downstream active head (DAH) [36–40,44] located at its downstream extremity. DAHs entraining LTBs drift at a speed about 0.8 in the streamwise direction and about 0.1 in the spanwise direction. In agreement with previous studies [39,40], these LTBs decay below $Re_g \approx 700$. At $Re = 850$ [Fig. 1(a)], all LTBs go in the same direction, therefore breaking the symmetry with respect to the spanwise direction. By contrast, LTBs go in both directions at $Re = 1050$ [Fig. 1(b)]. These states are respectively called one-sided and two-sided. As Re increases, LTBs joint to form a loose continuous network of oblique bands, and for $Re = 1200$ [Fig. 1(c)] DAHs practically cease to be seen. The pattern is strongly intermittent with turbulence intensity far from being uniform along the bands. At larger values of Re , the network narrows, $Re = 1800$ [Fig. 1(d)], and wide laminar voids disappear while regular patterns form, which can be understood as crisscrossed more acute ($\approx 25^\circ$) oblique turbulence modulations, $Re = 3000$ [Fig. 1(e)], similar to those obtained in circular Couette flow [10]. The amplitude of this modulation then decreases and the *featureless* regime eventually prevails for $Re \gtrsim 4000$ [Fig. 1(f)]. Properties of the flow deeper inside the uniformly turbulent, developed regime achieved at even larger values of Re are briefly reviewed in Ref. [45]. Figure 2 is a sketch of the bifurcation diagram

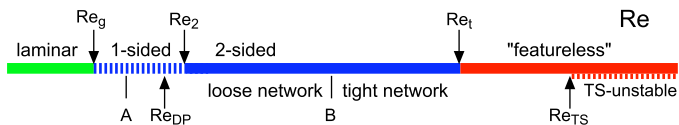


FIG. 2. Bifurcation diagram for plane channel flow as obtained in our simulations (corresponding values of Re_b between parentheses). Laminar flow is always recovered in the long-time limit for $Re < Re_g \approx 700$ ($Re \equiv Re_b$ up to Re_g). Event A corresponds to the onset of transversal splitting at $Re \approx 800$ ($Re_b \approx 795$). The extrapolated 2D-DP threshold is found at $Re_{DP} \approx 984$ ($Re_b \approx 905$). The transition from one-sided to two-sided propagation of LTBs takes place at $Re_2 \approx 1011$ ($Re_b \approx 924$). Event B marks the opening of laminar gaps in the turbulent branches, sufficiently long-lived to allow the development of DAHs. It takes place at $Re \approx 1200$ ($Re_b \approx 1012$). Finally, “featureless” turbulence is present for $R > Re_t \approx 3900$ ($Re_b \approx 1820$). The Tollmien-Schlichting instability threshold is at $Re_{TS} = 5772$ (analysis refers to laminar base flow, hence identical Re_b).

of channel flow indicating the different regimes illustrated above and anticipating the output of the quantitative study of phenomena developing for $800 \leq Re \leq 1200$ to be presented below.

Information from the statistics over the time series of typical global quantities is displayed as functions of Re or Re_b in Figs. 3 and 4. Transverse turbulent energies, $E_y(t) = \mathcal{V}^{-1} \int_{\mathcal{V}} u_y^2 d\mathcal{V}$ and $E_z(t) = \mathcal{V}^{-1} \int_{\mathcal{V}} u_z^2 d\mathcal{V}$, in Fig. 3(a) directly monitor the distance to the laminar base flow. Irregularities noted for $Re < 1200$ can be interpreted with the help of Figs. 1(a)–1(c). The rapid growth of E_y and E_z for $Re \leq 850$ is related to the increasing number of DAHs in the one-sided LTB regime. When $Re > 850$, the increasing fraction of LTBs with different orientations leads to a strong decrease in E_y and E_z until $Re \approx 1000$. Next, as Re increases, E_y grows again, owing to an increasing turbulent fraction while E_z slightly increases up to $Re \approx 1200$ before decreasing in the band-network regime where the global flow around LTBs is inhibited. The variations of the standard deviations of fluctuations, once normalized by their respective means, are remarkably correlated, as seen in Fig. 3(b). Their rapid growth as Re approaches $Re \approx 1000$ from above is reminiscent of the divergence of fluctuations observed for a phase transition at a threshold Re_2 precisely located later. Peaks at $Re = 725$ and $Re = 800$ mark the onset of longitudinal and transversal splittings to be examined below.

Further general observations about the transitional range as a whole can be extracted from our numerical results. Using a constant body force (mean applied pressure gradient), our numerical implementation of Navier-Stokes equations produces streamwise and spanwise net flux components U_m and W_m as time-fluctuating observables governed by (A5). In particular, the bulk Reynolds

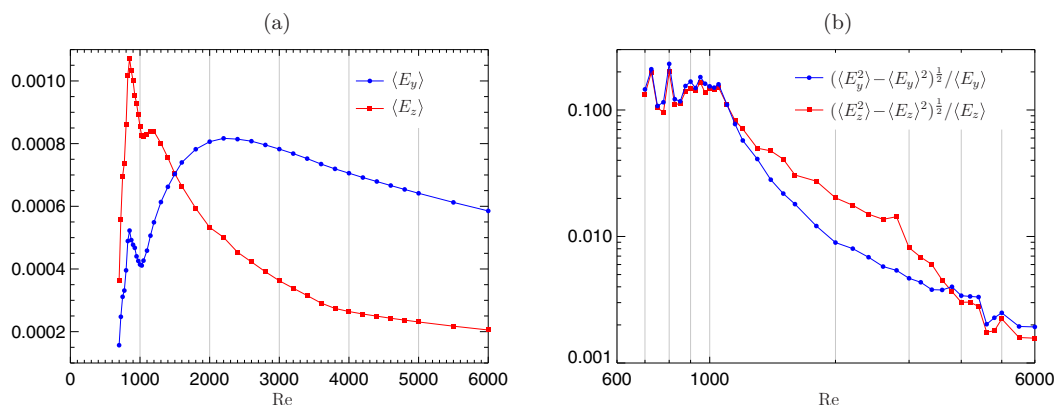


FIG. 3. Means (a) and relative standard deviations (b) of the wall-normal energy $E_y(t)$ and spanwise energy $E_z(t)$.

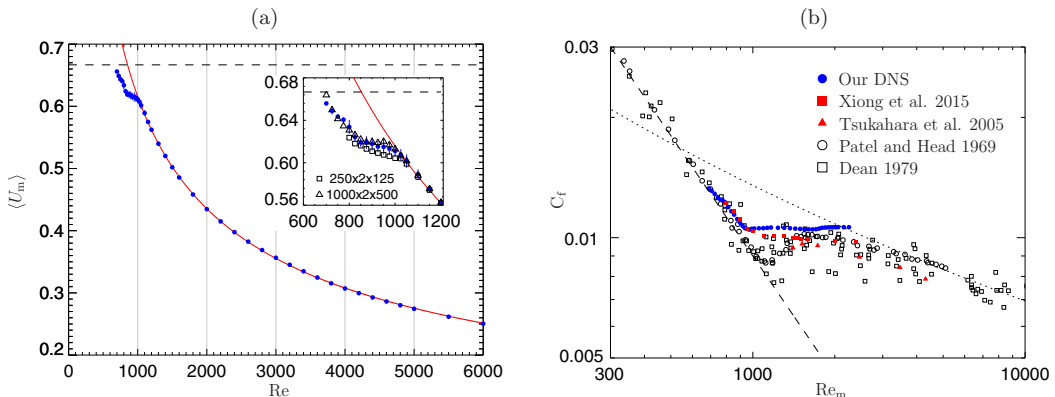


FIG. 4. (a) Average of streamwise bulk velocity $\langle U_m \rangle$ as a function of Re ; the solid line corresponds to the fit and the dashed line to laminar flow, $U_m^{\text{lam}} = 2/3$. Open symbols in the inset are for the different domain sizes. (b) Skin friction coefficient C_f as a function Re_b . Filled and open symbols are from DNSs (Tsukahara *et al.* [16], Xiong *et al.* [37]) and experiments (Patel and Head [47], Dean [46]), respectively. The dashed line is for laminar flow and the dotted line for the fully turbulent regime.

number $Re_b := \frac{3}{2}\langle U_m \rangle Re$ introduced earlier is obtained from the time average of U_m . Figure 4(a) displays $\langle U_m \rangle$ as a function of Re . Laminar flow corresponds to $U_m^{\text{lam}} = 2/3$. As soon as some turbulence is present, we get $\langle U_m \rangle < U_m^{\text{lam}}$ and, for Re above the one-sided regime, the observed decrease nicely fits an inverse square root over a large part of the transitional range. Using results for $Re \geq 1050$, we obtain $U_m^{\text{fit}} = w/\sqrt{Re}$ with $w \simeq 19.5$, and hence $Re_b \approx \frac{3}{2}w\sqrt{Re}$. Turning to wall units, the friction velocity U_τ and the friction Reynolds numbers Re_τ are obtained in our formulation as $U_\tau^2 = \tau_w = 2/Re$ and $Re_\tau = \sqrt{2Re}$, relation (A11). This means that Re_τ and Re_b are roughly proportional as long as the flow remains textured, before entering the developed regime where Re_τ then grows as a function of Re_b at a slightly smaller rate (exponent $\simeq 0.88$ [45]). This behavior is directly reflected in the variation of the skin friction coefficient C_f with Re_b shown in Fig. 4(b). Here, we have $C_f := \tau_w / \frac{1}{2}\langle U_m \rangle^2 = 4 / (Re \langle U_m \rangle^2)$ (see Appendix A). As soon as some turbulence is present, C_f deviates from its laminar expression $9/Re_b$, remains close to it in the one-sided regime, and next changes to a near plateau dependence as soon as it enters in the two-sided regime, as expected from the variation of $\langle U_m \rangle^2$ as Re^{-1} in the corresponding Re range. In our simulations, this plateau extends up to the transition to fully developed turbulent channel flow marked by a dotted line in Fig. 4(b), theoretically expressed as $Re_b = \frac{3}{\sqrt{2C_f}} \exp[0.41(\sqrt{2/C_f} - 2.4)]$ [45,46]. This plateau is better defined than in earlier experiments [46,47] and simulations [16,37] also shown in the picture. It indicates that, above Re_2 , the transition to turbulence develops at a nearly constant dissipation rate $\langle \epsilon_m \rangle$, as stems from relation (A12). In the upper transitional range $Re \gtrsim 4000$, i.e., $Re_b \gtrsim 1850$, the trend suggested by our data points seems to overestimate C_f as predicted for the fully turbulent regime [45] (dotted line). This is presumably due to a lack of resolution close to the wall at such high values of the Reynolds number. A detailed quantitative study of the transition to the “featureless” regime around Re_c , beyond the preliminary result in Ref. [48] indicated in Fig. 2, is left to future work.

III. SYMMETRY-RESTORING BIFURCATION

Laminar-turbulent patterns below $Re = 1200$ were examined to better understand the symmetry-restoring bifurcation observed at increasing Re . Processes involved in the dynamics are illustrated in Fig. 5. The local spread and decay of turbulence respectively stem from splittings and collisions of LTBs with either identical or opposite orientations. Figure 5(a) shows the nucleation of a new band by *longitudinal splitting* of an LTB at its tail. The active region is downstream and the splitting

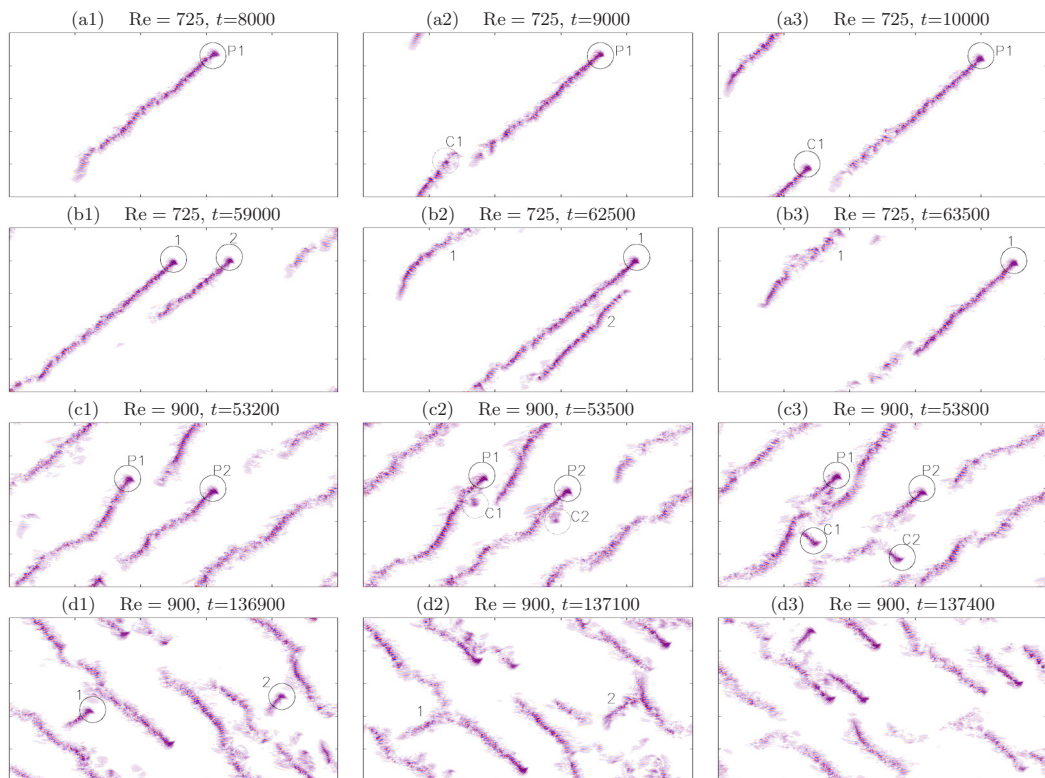


FIG. 5. (a) Longitudinal splitting. (b) Longitudinal collision. (c) Transversal splitting. (d) Transversal collision. The same quantity as in Fig. 1, $u_y(x, 0, z; t)$, is displayed in a comoving frame with velocity $(u_x^{(f)}, u_z^{(f)}) = (0.8, 0.1)$. Circles locate DAHs to be followed and numbers identify bands, “P” and “C” stand for parent and child, respectively. See also videos in the Supplemental Material [43].

takes place upstream where the turbulence level is always weaker than near the DAH, contrary to what happens for puffs in pipe flow [20,49]. When two parallel LTBs collide (*longitudinal collision*), following the large-scale flow around them [37,38,40], the upstream faster LTB catches the downstream LTB that disappears as in Fig. 5(b). At larger Re, another splitting process here called *transversal* can take place along an LTB: A turbulent “bud” appears on the side of an LTB and forms an off-aligned turbulent branch as in Fig. 5(c). Finally, when the DAH of a new LTB collides an LTB with a different orientation (*transversal collision*), the attacker most often dies in the collision [Fig. 5(d)]. The occurrence of transversal splitting causes the spread of turbulence to be a genuinely two-dimensional process. Transversal splitting has also been observed in plane Couette flow and considered essential to the development of laminar–turbulent patterns [50]. Although transversal splittings are observed for $Re \geq 800$, one propagation direction remains dominant up to threshold Re_2 .

This spanwise-symmetry restoring bifurcation from one-sided flow to two-sided flow can be understood using a simple prey-predator model for the densities X_{\pm} of two species of LTBs, left propagating and right propagating:

$$dX_+/dt = aX_+ - bX_+^2 + cX_- - dX_+X_-, \quad (1)$$

$$dX_-/dt = aX_- - bX_-^2 + cX_+ - dX_+X_-. \quad (2)$$

By construction, these equations incorporate the built-in spanwise symmetry of the system and each term corresponds to a process in Fig. 5. Coefficient a represents the *longitudinal* splitting rate [Fig. 5(a)]. The *transversal splitting* rate c [Fig. 5(c)], the natural control parameter, is assumed to increase with Re according to the observations ($c > 0$ for creation of X_{\pm} out of $X_{\mp} \neq 0$, hence $c \geq 0$ for $\text{Re} \gtrsim 800$, event A in Fig. 2). Coefficients b and d account for the turbulence-level decrease by the collision between LTBs of either the same [Fig. 5(b)] or different [Fig. 5(d)] orientations. For collisions between differently oriented LTBs, the term $-dX_+X_-$ models the decay rate of one of the species X_{\pm} taken as proportional to the cross section of LTBs of the opposite kind X_{\mp} . Coefficient d , which is weakly dependent on Re and a function of the speed of colliding LTBs, is assumed constant, as well as b parametrizing a logistic self-interaction for predation among LTBs with the same orientation, i.e., $-bX_{\pm}^2$. A reduced cross section and a very small relative velocity between LTBs of the same kind suggest $b \ll d$. In contrast with works elaborating on reaction-diffusion models devised to account for local interactions in transitional flows [51,52], our approach is Landau-like and deals with global observables minimally coupled by purely phenomenological coefficients.

The analysis of the model is straightforward when considering the total amount of turbulence $S = X_+ + X_-$ and the degree of asymmetry $A = X_+ - X_-$ as working variables. The equations for these variables become

$$\frac{dS}{dt} = (a + c)S - \frac{1}{2}(b + d)S^2 - \frac{1}{2}(b - d)A^2, \quad (3)$$

$$\frac{dA}{dt} = (a - c)A - bSA. \quad (4)$$

The two-sided regime labeled “**” corresponds to $A = 0$, while $A \neq 0$ implies the dominance of one propagation direction. “ $A_{**} = 0$ ” solves (4) in all circumstances. Using (3), the symmetrical fixed point is then given by

$$S_{**} = \frac{2(a + c)}{b + d}, \quad A_{**} = 0. \quad (5)$$

This fixed point has eigenvalues (s_S, s_A) with $s_S = -(a + c) < 0$ and $s_A = [a(d - b) - c(d + 3b)]/(b + d)$. The symmetric solution is then stable as long as $s_A < 0$; hence, $c > c_c = a(d - b)/(d + 3b)$ when $b < d$ as assumed from the observations. The two-sided regime is then stable for large Re and becomes unstable below a threshold corresponding to c_c .

The one-sided regime labeled “*” corresponds to $A \neq 0$ at steady state (fixed point); hence, from (4) and next from (3)

$$S_* = \frac{a - c}{b}, \quad A_*^2 = \frac{(a - c)(d + 3b)(c_c - c)}{b^2(d - b)}. \quad (6)$$

This analysis shows that the system experiences a standard supercritical pitchfork bifurcation toward asymmetry by decreasing c . At $c = c_c$ as previously defined, (S_{**}, A_{**}) becomes unstable and is replaced by $(S_*, \pm A_*)$, which is stable for $c < c_c$ as expected. Figure 6(a) displays the bifurcation diagram of model (3) and (4) with splitting rate c taken as the control parameter, and $a = 10^{-4}$, $d = 10$, $b = d/10$. The thick line represents the total turbulence amount S given by $S_* = (a - c)/b$ below c_c and $S_{**} = 2(a + c)/(b + d)$ above. Thin lines correspond to X_{\pm} . Dashed lines correspond to the unstable solutions (the dashed branch for $c > a$ is furthermore irrelevant to the present problem since it leads to negative values of X_-).

Experimental support to the model is displayed in the boxed region in Fig. 6(b). The total transverse perturbation energy $E_y + E_z = E_{2D}$ is taken as a proxy for S . The mean spanwise velocity component $W_m = \mathcal{V}^{-1} \int_{\mathcal{V}} u_z d\mathcal{V}$ is interpreted as an instantaneous measure of the degree of asymmetry A because it cancels out statistically when symmetry is restored at high Re , i.e., $\langle W_m \rangle = 0$, where $\langle \cdot \rangle$ represents time average. Notice that the standard deviation of E_{2D} is multiplied by 6 and both $\langle W_m \rangle$ and its standard deviation are divided by 4 so that variations of the observables can be more easily compared. As long as transversal splitting is negligible, $\langle E_{2D} \rangle$ and $\langle W_m \rangle$ increase

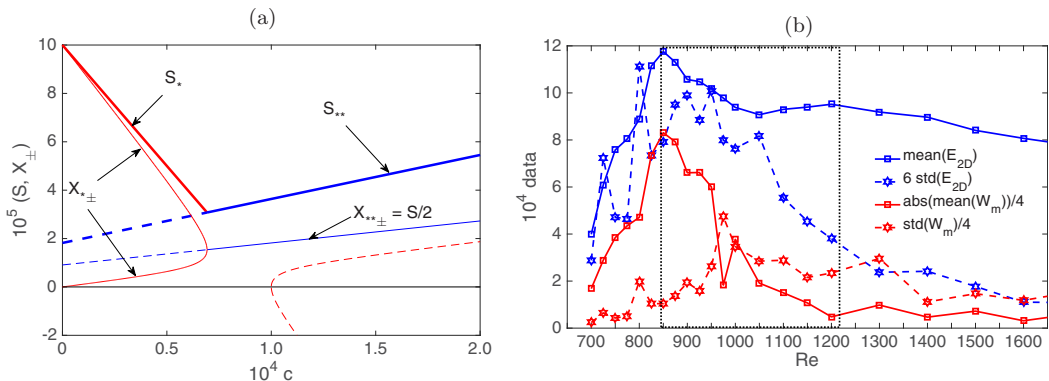


FIG. 6. Transition from one-sided to two-sided flow. (a) Model. (b) Numerical simulation.

with the mean length of LTBs. The two orientations correspond to $\langle W_m \rangle$ with opposite signs. Periodic spanwise boundary conditions leave open the possibility of having $W_m \neq 0$ as a result of symmetry breaking. The case of an experimental system with solid lateral boundaries forbidding such a net transverse flux is considered later in Sec. V. In Fig. 6(b), we only display $|\langle W_m \rangle|$ since at steady state, depending on the orientation of the LTBs, $\pm |\langle W_m \rangle|$ are equally possible. Both $\langle E_{2D} \rangle$ and $|\langle W_m \rangle|$ reach their maximum values for $Re \approx 850$, which can be understood as when transversal splitting—not observed below $Re = 800$ —becomes significant. For $Re > 850$, our two observables follow the trend suggested by the model: $\langle E_{2D} \rangle$ decreases roughly linearly as Re increases up to $Re \approx 1000$ and slowly grows beyond, in agreement with Eqs. (5) and (6). Likewise, $|\langle W_m \rangle|$ decreases rapidly to zero, similar to A_* , as indicated by the fact that the standard deviation becomes larger than the mean at $Re \approx 1000$. For larger Re outside the box, the system enters a developed two-sided regime where the model, designed to account for the symmetry-restoring bifurcation, becomes insufficient. Inside the box, this oversimplified formulation well captures the phenomenology of the transition at a qualitative level.

The transition is then understood by assuming that parameter c measuring the transversal splitting rate increases with Re . The analysis above shows that $c_c \simeq a$ assuming that $b \ll d$, as stems from our observations. Furthermore, in the range $850 \leq Re \leq 1200$, the variations of S and A around c_c are consistent with those of the turbulent energy and the spanwise mean velocity, respectively. In fact, the deviation of $\langle U_m \rangle$ away from its behavior in the two-sided regime fitted as $U_m^{\text{fit}} = w/\sqrt{Re}$ in Fig. 4(a) is a proxy for the change of total amount of turbulence at the symmetry-restoring bifurcation. As displayed in Fig. 7, this variation is linear close to the bifurcation point $Re_2 \simeq 1011$, in agreement with the predictions of the model. As can be seen in the inset of Fig. 4(a) and in Fig. 7, the current domain size is appropriate to obtain this threshold.

IV. BEHAVIOR ABOVE Re_2

Beyond Re_2 and up to entrance in the tight-banded pattern regime [Fig. 1(e)], channel flow exhibits a spatiotemporal intermittent behavior [Figs. 1(c) and 1(d)], strongly reminiscent of DP above the threshold. The work of Sano and Tamai [35] focusing on the critical properties of turbulence decay in a DP context [28] naturally suggests studying this Reynolds number range in terms of turbulent fraction F_t . This in turn relies on the identification of appropriate laminar and turbulent local states, based on observables that vary sufficiently sharply in space to define the respective domains properly, allowing a precise measurement of their relative occupancy fractions. Figure 8 displays four possible candidates, the three velocity components in the midgap plane $y = 0$, and the mean transverse perturbation energy $E_{2D}(x, z; t) = \frac{1}{2} \int_{-1}^1 (u_y^2 + u_z^2) dy$ around an LTB at $Re = 700$. In-plane components u_x and u_z display a large-scale, slowly decaying structure around

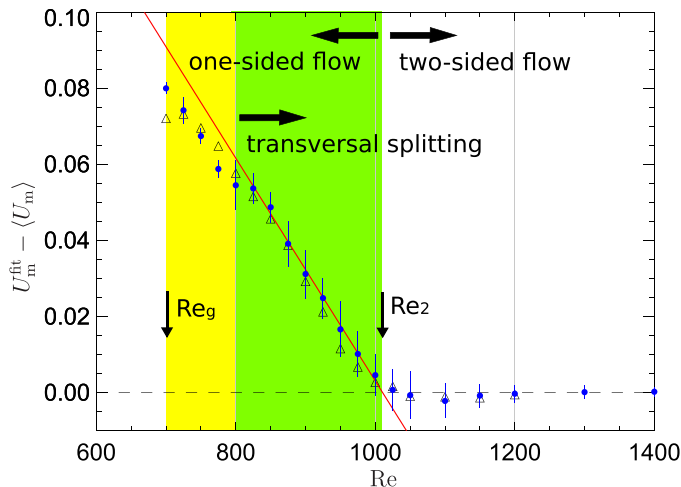


FIG. 7. Departure of observed streamwise mean flow $\langle U_m \rangle$ from the value predicted by the law $U_m^{\text{fit}} = 19.47/\sqrt{\text{Re}}$, solid line in Fig. 4(a). Fitting the data against a straight line for $850 \leq \text{Re} \leq 1000$ yields $\text{Re}_2 \simeq 1011$. Triangles are for the larger domain $1000 \times 2 \times 500$.

the LTB. By contrast, u_y sharply discriminates nonlaminar flow regions. E_{2D} is slightly less close fitting due to the limited contribution of the component u_z . Accordingly, the absolute value of the wall-normal velocity on the midplane $|u_y(x, 0, z)|$ will be used to evaluate F_t . However, inside LTBs, u_y displays small-scale oscillations associated with the presence of streamwise vortices, which produces narrow regions with $|u_y(x, 0, z)| \approx 0$ that must not be counted as laminar. Accordingly, the field $|u_y(x, 0, z)|$ has to be smoothed beforehand, here by simple box averaging over cells of

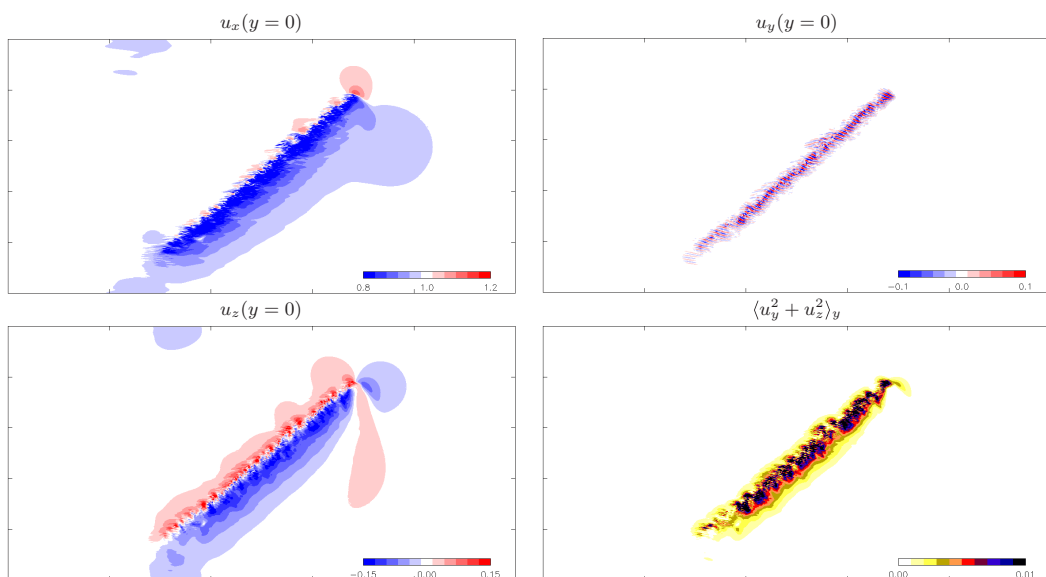


FIG. 8. Possible candidates for the determination of the turbulent fraction illustrated by 2D images of the same localized turbulent band at $\text{Re} = 700$. The flow is from left to right and the downstream active head is in the upper right corner in each panel. Domain size is 500×250 .

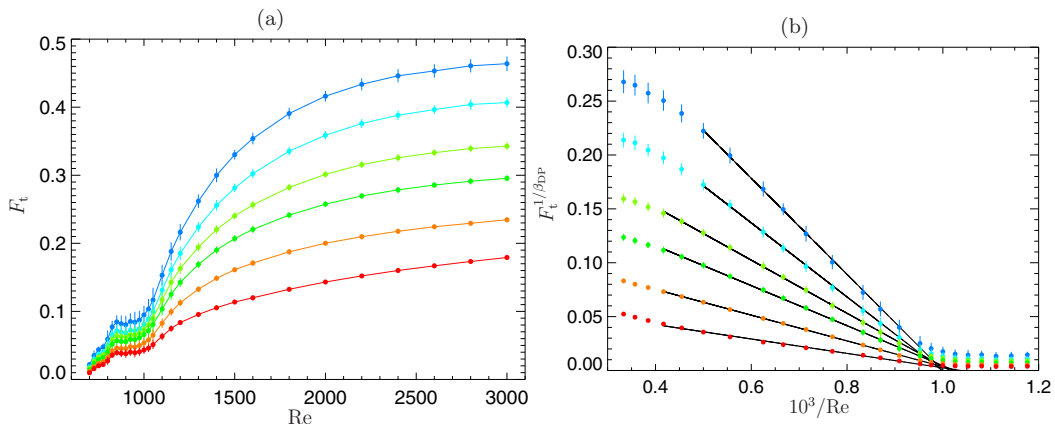


FIG. 9. F_t for different w . From the bottom to the top: $w = 0$ (no filtering, red), 4δ , 8δ , 12δ , 20δ , and 40δ (blue). (a) F_t as a function of Re . (b) $F_t^{1/\beta_{DP}}$ as a function of $1/Re$ with $\beta_{DP} = 0.583$.

size $w \times w$, and next thresholded using the ‘‘moment-preserving’’ procedure [53], as explained in Appendix B.

The variation of F_t as a function of Re is displayed in Fig. 9(a) for $700 \leq Re \leq 3000$ and for w varying between 0 (no filtering) and 40δ . For all values of w , similar variations are observed and one readily identifies the different stages illustrated in Fig. 1: one-sided growth for $Re \leq Re_2 \simeq 1011$, with a clear change of regime for $Re \approx 850$ as transversal splitting sets in, before a rapid increase akin to a power-law growth as Re increases in the symmetry-restored regimes [Figs. 1(b)–1(d)] up to the tight banded pattern regime [Fig. 1(e)].

The consistent square-root-like behavior is reminiscent of the growth of the order parameter of DP beyond threshold. In line with the idea that the critical properties of the stochastic DP process are relevant for channel flow, as put forward by Sano and Tamai, we first test the plausibility of exponent $\beta_{DP} \simeq 0.583$ to describe the variation of the turbulent fraction with the relative distance to threshold. Figure 9(b) therefore displays $F_t^{1/\beta_{DP}}$ as a function of $1/Re$. The linear behavior of the plots for different values of w , systematically extrapolating to zero for around $Re \approx 1000$ ($1000/Re \approx 1$), therefore strongly supports the expected behavior of F_t as if it were produced by a 2D-DP process. From the least-square fits, the straight lines in Fig. 9(b), it is seen that some filtering is needed to eliminate spurious small-scale oscillations of $u_y(x, 0, z)$ since raw data ($w = 0$, red data points) does not behave so satisfactorily. On the other hand, strong filtering ($w \geq 20$) leads to a reduction of the range where a good linear fit is obtained ($1050 \leq Re \leq 2400$ for $w \leq 12\delta$ and $1050 \leq Re \leq 2000$ for $w = 20\delta$ and 40δ). To further develop the quantitative analysis, we choose the best compromise, which seems to be $w = 12\delta$, i.e., the largest filtering possible in the widest Re interval with the expected property.

In these conditions, a direct fitting over the interval $1050 \leq Re \leq 2400$ has been attempted against the function $F_t = B(1 - Re_{DP}/Re)^\beta$ with B , Re_{DP} , and β as fitting parameters. We proceeded to a least-square minimization of the error $Err^2 = \frac{1}{N} \sum_{n=1}^N [F_{t_n} - B(1 - Re_{DP}/Re_n)^\beta]^2$, where N is the number of values Re_n of Re entering the fit and F_{t_n} is the corresponding measured mean turbulent fraction. Figure 10(a) displays the minimum error as a function of β , pointing to $\beta \approx 0.58$, while Figs. 10(b) and 10(c) display similar results for $B \approx 0.45$ and $Re_{DP} \approx 984$ as best fitting values, respectively. Following this approach, the estimate for β turns out to be close to the theoretical value $\beta_{DP} = 0.583$ that served as our initial guess in Fig. 9(b). The error curves in each case, however, indicate that the optima are not sharply defined. Unfortunately, these estimates cannot be improved, mainly because the critical point cannot be approached sufficiently closely. This also justifies that

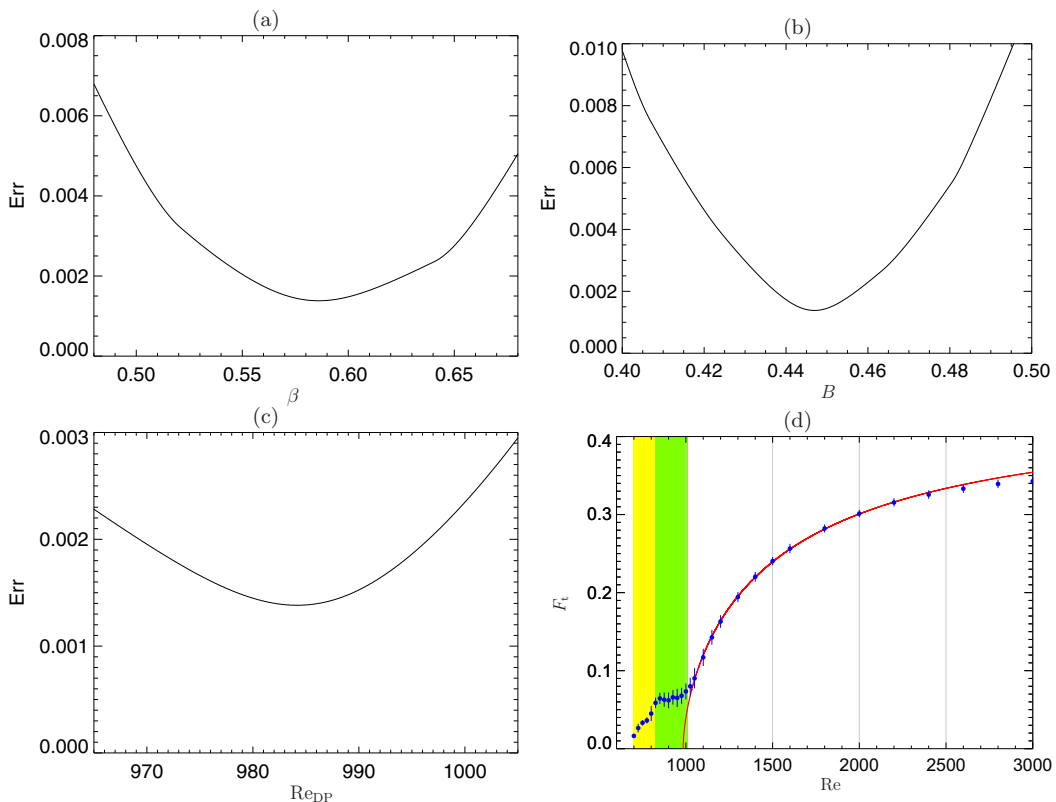


FIG. 10. [(a)–(c)] Minimum of Err as a function of the different fit parameters for F_t with $w = 12\delta$ and control parameter $1/Re$. (a) Exponent β . (b) Amplitude B . (c) Threshold Re_{DP} . In these panels, the error is displayed as a function of one fitting parameter, the two other being supposed fixed at their optimal value. (d) Turbulent fraction F_t as a function of Re and its fit against the theoretical expression given in Sec. IV.

we did not try to adjust the other critical parameters related to space-time correlations since they are discriminating solely in an arbitrarily close neighborhood of Re_{DP} .

Our results, used to draw the fitting line in Fig. 10(d), therefore point toward a plausible universal DP behavior for large enough turbulent fraction, a behavior inevitably truncated before criticality by a crossover to a different decay regime as Re decreases. As a matter of fact, the turbulent fraction becomes so small that laminar gaps open along oblique arms of the fluctuating laminar-turbulent network, which produces the development of DAHs—original to channel flow—so that the DP regime is superseded by the LTB-dominated regime and, as Re decreases even more, to the symmetry-breaking bifurcation below which turbulence decay takes up a novel turn.

V. DISCUSSION AND CONCLUDING REMARKS

Apart from a few illustrations of the laminar-turbulent patterning in the upper transitional range of channel flow in Figs. 1(e) and 1(f), our results all relate to its lower part featuring the decay to laminar flow where a DP scenario with universal properties expected for two-dimensional systems has been put forward [35], while sustained LTBs have been observed at values of Re lower than the measured DP critical point [36–42]. The first result comes in support of a theoretical conjecture by Pomeau [27] based on the recognition that the flow can be locally in one of the two possible states, turbulent or laminar. Furthermore, in the transitional range, developing turbulence presents

itself as a contamination of the laminar state, locally linearly stable and therefore *absorbing*, by a highly fluctuating, unstable, chaotic *active* state. This framework is directly derived from a statistical-physics approach where the key concept is the thermodynamic limit of infinitely wide systems at statistically steady state (here nonequilibrium steady state). Though experiments and simulations are performed in domains and for durations somewhat far from the thermodynamic-limit conditions (with Ref. [33] as a possible exception), the question of what we may infer on general grounds from our results is relevant.

Let us first notice that comparisons with laboratory experiments and computer simulations are made difficult because of the several possibilities chosen to drive the flow, either generated by a fixed pressure gradient (or given average friction at the walls) or a constant mean streamwise flow rate. Though it is generally admitted that the results should be statistically identical at the thermodynamic limit, quantitative correspondence between different works is not easy to establish, and first of all with respect to how Re is defined owing to what is controlled and what is measured. Here, we fix the mean pressure gradient (fixed bulk force f) and use the computed centerline velocity of the corresponding laminar flow U as speed unit, while the half-distance h between the plates is taken as length unit and h/U as time unit. The definition of $Re = Uh/\nu$ follows. If wall units are preferred, e.g., in Ref. [16], one gets $Re_\tau = \sqrt{2Re}$ as derived in Appendix A. In the laminar regime, the mean flow rate is $U_m = \frac{2}{3}U$ and the Reynolds number made out of it: $Re_m = U_m h/\nu = \frac{2}{3}Re$ is frequently used. However, when the flow is not fully laminar, the measured mean flow rate $\langle U_m \rangle$ decreases below its nominal value $2/3$ (Fig. 7). Accordingly, the Reynolds number constructed using $\langle U_m \rangle$ is not a control parameter but an observable that has to be determined by averaging u_x over space and time. This leads us to define $Re_b = \frac{3}{2}\langle Re_m \rangle = \frac{3}{2}\langle U_m \rangle h/\nu$. With this definition, when the flow is fully laminar, $Re_b \equiv Re$ and, accordingly, the linear instability threshold is $Re_{TS} = 5772$ [3]. Keeping $\langle U_m \rangle$ strictly constant, as done in some numerical experiments and only approximately achieved in the laboratory, is therefore a different experiment in which the applied pressure gradient is unknown and fluctuating. All in all, our results in Fig. 1 are consistent with those found in the literature when expressed in terms of Re_b , especially those in Refs. [16,40] or even in Refs. [18,54].

Our main contention is that the previously mentioned conflicting experimental observations about DP universality and the existence of LTBs can be reconciled provided that it is recognized that the DP scenario cannot be followed down to its critical point. We have shown that, when the turbulent fraction is small enough, processes develop which are not present in other systems where DP universality is observed: As Re is slowly decreased, the flow evolves from the weakly intermittent loose banded pattern regime, Fig. 1(d), to the strongly intermittent continuous network regime, Fig. 1(c). Further decreasing Re induces the opening of laminar gaps along the turbulent branches, here called *splittings*, and the formation of LTBs terminated by DAHs constitutive of the two-sided LTB regime, Fig. 1(b). At first, the intermittent expansion and recession of turbulence is two dimensional in the plane of the flow owing to comparable rates for transversal and longitudinal splittings, but the rate of transversal splittings decreases with Re faster than that of longitudinal splittings, which implies a change to one-sided LTB propagation, i.e., a symmetry breaking due to a deficit of regeneration of one of the two LTB species at a local scale. In the long term, the rate difference indeed brings about a global dominance of one orientation over the other and a mostly one-dimensional expansion and recession of turbulence. In this respect, the cases of Waleffe flow [33] and plane Couette flow [34] appear different. In these two cases, laminar gaps also open through splittings, longitudinal and transversal, along the turbulent segments forming the fluctuating laminar-turbulent network but the upstream-downstream distinction does not make sense. Close to Re_g , the turbulent patches accordingly take the form of fluctuating short oblique straight segments, v-shaped spots, or x-shaped spots [33, Fig. 2] with dynamics profoundly different from that of LTBs equipped with DAHs. As a result, the turbulent fraction can then decrease indefinitely according to 2D-DP universality, down to Re_{DP} that is reached before any symmetry-breaking bifurcation has a chance to take place, presumably because the longitudinal and transversal splitting rates remain comparable as Re decreases. By contrast, specificities of channel flow prevent the observation of a

complete $2D$ -DP scenario and the origin of this *imperfection* is fully characterized as the result of an unavoidable symmetry-breaking bifurcation when the turbulent fraction becomes small enough, before the expected Re_{DP} is reached.

We now focus the discussion on two main points: the variation of the turbulent fraction in the range $1050 \leq Re \leq 2400$ in connection with the DP scenario above the symmetry-breaking bifurcation, and the nonzero mean transverse flow in the symmetry broken regime, $Re \leq Re_2$, its observability at the thermodynamic limit or, at the opposite, in laterally bounded finite-width channels.

For the conceptual reasons already evoked, DP is relevant *as a process* in the lowest transitional range. In its simplest formulation used to typify the universality class, a single contamination probability is needed to control the transition but the nature of physical mechanisms involved and their dependence on the Reynolds number are not known. The expectation for universality rests on the Janssen-Grassberger conjecture [28] stipulating in particular that the absorbing state is unique, the interactions are local, and there are no weird parasitic effects such as quenched disorder, which is implicitly assumed if Pomeau's educated guess is valid. Strictly speaking, the question whether the decay of turbulence in channel flow follows $2D$ -DP universality is void since the critical regime—the immediate neighborhood of the threshold—cannot be entered, but results presented in Sec. IV suggest a positive answer if we accept loosening this restriction (Fig. 10).

This argument, however, hides a difficulty since, as already mentioned, the relation between the chosen external control parameter and the internal control parameter, the effective contamination probability generated by stochastic processes at the scale of a few MFUs, is not known. On general grounds, the critical behavior is not sensitive to the choice of the external control parameter in an asymptotically close vicinity of the critical point while departures from universality become conspicuous at variable distances from the threshold depending on that choice. In the previously reported cases, the variation of the turbulent fraction as a function of the Reynolds number deviates from the expected power law dependence beyond a relative distance ϵ to the critical point $\approx 10^{-2}$ for quasi- $1D$ plane Couette flow [31, Fig. 2], or $\approx 10^{-3}$ for quasi- $2D$ Waleffe flow [33, Fig. 4]. For channel flow, the universal behavior of the turbulent fraction is reported for $\epsilon \lesssim 0.1$ in [35, Fig. 3], but the experimental conditions do not permit access to the LTB regime. By contrast, taking advantage of a streamwise periodically continued domain, our approach leaves sufficient time for turbulent patches to rearrange into LTBs, which truncates the DP behavior above threshold [55]. Our most striking finding is that, characterizing the flow by its natural control parameter Re , the turbulent fraction then varies in accordance with universality over a surprisingly wide interval from below $Re \approx 2400$ nearly down to Re_2 where the dynamics becomes controlled by LTBs. When expressed in terms of $\epsilon = 1 - Re_{DP}/Re$ with $Re_{DP} = 984$ as the extrapolated threshold, this range extends over $0.07 \lesssim \epsilon \lesssim 0.6$ [Figs. 9(b) and 10(d)]. At this point, it is fair to add that other possibilities for the external control, namely using Re_τ or Re_b in principle equivalent in the neighborhood of the threshold, perform badly at some distance above threshold, not even permitting us to detect a neat power-law variation over such a wide interval. The physical meaning of Re_τ or Re_b implies an averaging over the flow in a strongly inhomogeneous spatiotemporally intermittent state, which might explain that the probabilities issued from the dynamics at the MFU scale are less straightforwardly parameterized using them than using Re (or $1/Re$).

Let us now turn to the symmetry breaking observed at decreasing Re and studied in Sec. III. Elementary events involved in the dynamics of LTBs were described in detail (Fig. 5). A satisfactory simple phenomenological model was developed then in the spirit of Landau theory to account for the bifurcation at a qualitative and semiquantitative level. Extrapolating our results in a finite-size domain with periodic boundary conditions to a laterally unbounded system (thermodynamic limit), when transversal splitting is negligible ($Re \lesssim 800$), one-sided propagation is expected because for Re low enough, any transversal collision destroys one of the colliders [Fig. 5(d)], and, as seen in the movies at low Re [43], the transient evolution of sparse turbulence follows a majority rule. At short times, a patchwork of domains with one or the other dominant orientation forms, with

transversal collisions concentrated along the domain boundaries. At longer times, a ripening process develop during which domains compete with each other, locally applying the majority rule so that, in the very long time limit at very low LTB density, one can figure out an asymptotic steady state which is mostly uniformly oriented. Residual LTBs are then moving nearly at the same speed, along the same direction, and interact only through longitudinal splittings and collisions [Figs. 5(a) and 5(b)], maintaining a state free of transversal collisions. Such a regime is expected to persist down to Re_g , below which it decays, much like in pipe flow [20], due to the predominance of longitudinal destructive collisions over expanding turbulence through splittings to be discussed in a future publication [56].

The difficulty with this picture is that, on general grounds, such symmetry breaking is associated to with large-scale flow with a transverse component corresponding to a net, fluctuating, spanwise mean flux with nonzero average (W_m). In systems with periodic spanwise boundary conditions, symmetries do not forbid the existence of such a flow. Close to the bifurcation point, for $Re < Re_2$ when transversal splitting plays a significant role, the patchwork alluded to above can reach a statistically steady state with $\langle W_m \rangle \neq 0$ but reduced by compensations between patches of different orientations, whereas for $Re > Re_2$ one gets $\langle W_m \rangle \approx 0$ with substantial fluctuations; see Fig. 6(b). These are the characteristics of an order parameter apt to quantify the symmetry-breaking bifurcation. From the observations reported in the previous paragraph, these properties are expected to hold also as t goes to infinity in a spanwise unbounded system (thermodynamic limit).

In finite-width channels with impervious lateral walls, any net spanwise mean flow W_m is not permitted. In laboratory experiments where this condition applies, the one-sided regime has been observed [41,42] but, in contrast with our simulations where LTBs drift obliquely, after an initial transient stage during which the flow equilibrates, they are advected strictly along the streamwise direction. This means that an additional spanwise pressure wave accompanies the passing of an LTB, producing a spanwise mean flow component able to deviate it, thus compensating for the W_m that it would naturally generate. Rigid lateral walls are obviously able to withstand such pressure fluctuations as LTBs pass by. Only simulations specially designed to implement the corresponding no-slip lateral boundary conditions, e.g., with spanwise Chebyshev polynomials [24], would permit a detailed account of the LTB propagation in the one-sided regime. However, while keeping spanwise periodic boundary conditions, one can think of correcting our governing equations for an additional spanwise fluctuating bulk force generating a mean transverse flow sufficient to compensate the drift of LTBs and statistically maintain a strictly streamwise propagation. Such a work remains to be done but could give hints on the one-sided regime in realistic experimental conditions, owing to the obvious robustness of LTBs.

Two complementary studies are in progress, above and below the range of Reynolds numbers considered in this work: One is dedicated to the decay of the one-sided regime in a domain $1000 \times 2 \times 500$ or larger [56] and the other is focused on the onset of the laminar-turbulent patterning via standard Fourier analysis rather than turbulent fraction determination [48, see Fig. 4 for preliminary results].

By way of conclusion, the introduction of concepts and methods of statistical physics, and notably directed percolation, have put stress on universal features of the transition to and from turbulence in wall-bounded shear flows. All over the spatiotemporally intermittent regimes along the transitional range of channel flow, laminar-turbulent coexistence with a high level of stochasticity legitimates Pomeau's views [27] about the decay of turbulence at Re_g as a process in the $2D$ -DP universality class. We have shown that this claim is, however, only partly fulfilled because a specific phenomenon comes and renders the full scenario imperfect: Spanwise symmetry is broken due to a sensitive balance between local processes (longitudinal versus transversal splittings) with rates depending on Re in different ways, ending with recession and expansion of turbulence becoming mostly one-dimensional before $2D$ -DP criticality has a chance to be observed. In turn, this symmetry breaking is an event that could be well understood within the standard framework of dynamical systems and bifurcation theory, bringing an original perspective to the debated issue of universality versus specificity in the transition to turbulence of wall-bounded flows.

ACKNOWLEDGMENTS

We would like to thank Y. Duguet (LIMSI, Orsay, France) for interesting discussions about the problem. Referees should also be thanked for their comments that helped us improve our work. Travel support is acknowledged from CNRS and JSPS through the collaborative project TRANSTURB. This work was specifically supported by JSPS KAKENHI (JP17K14588), NIFS Collaboration Research program (NIFS16KNSS083, NIFS19KNSS124), and Information Technology Center, University of Tokyo.

APPENDIX A: SYSTEM AND NUMERICAL PROCEDURES

We consider the flow between two parallel walls driven by a time-independent body force, usually called channel flow or plane Poiseuille flow. The equations governing the velocity field \mathbf{u} are as follows:

$$(a) \quad \nabla \cdot \mathbf{u} = 0, \quad (b) \quad \frac{\partial \mathbf{u}}{\partial t} + (\mathbf{u} \cdot \nabla) \mathbf{u} = -\frac{1}{\rho} \nabla p + \nu \Delta \mathbf{u} + f \hat{e}_x, \quad (A1)$$

where $\rho = \text{const.}$ is the density, ν is the kinematic viscosity, and f is the body force specific density. The unit vector in the streamwise direction x is denoted as \hat{e}_x . The y and z axes are along the wall-normal and spanwise directions, respectively. All fields are assumed in-plane periodic and the velocity fulfills the usual no-slip boundary conditions at the walls.

The center-plane velocity of the corresponding laminar flow is $U = fh^2/2\nu$, where $2h$ is the distance between the walls. The Reynolds number is defined as $\text{Re} = Uh/\nu = fh^3/2\nu^2$. Using h and U as distance and velocity units, and h/U as the time unit, where all variables below are assumed dimensionless without a notational change, the equations governing the velocity field $\mathbf{u}(x, y, z, t)$ are as follows:

$$(a) \quad \nabla \cdot \mathbf{u} = 0, \quad (b) \quad \frac{\partial \mathbf{u}}{\partial t} + (\mathbf{u} \cdot \nabla) \mathbf{u} = -\nabla p + \frac{1}{\text{Re}} \Delta \mathbf{u} + \frac{2}{\text{Re}} \hat{e}_x. \quad (A2)$$

In practice, these equations are rewritten for the wall-normal velocity component $u_y(x, y, z, t)$ and the wall-normal vorticity $\omega_y(x, y, z, t) = (\nabla \times \mathbf{u})_y$ obtained by applying $\nabla \times$ and $\nabla \times \nabla \times$ to (A2b) and keeping its y component [2]:

$$(a) \quad \frac{\partial \omega_y}{\partial t} = (\nabla \times \mathbf{N})_y + \frac{1}{\text{Re}} \Delta \omega_y, \quad (b) \quad \frac{\partial \Delta u_y}{\partial t} = -(\nabla \times \nabla \times \mathbf{N})_y + \frac{1}{\text{Re}} \Delta \Delta u_y, \quad (A3)$$

where $\mathbf{N} = \mathbf{u} \times \boldsymbol{\omega}$.

The full solution requires additional equations for in-plane averaged velocity fields. We define the auxiliary fields $\phi_x(y, t)$ and $\phi_z(y, t)$ as $\partial_y \phi_x = \langle u_x \rangle_{xz}$ and $\partial_y \phi_z = \langle u_z \rangle_{xz}$, where $\langle g \rangle_{xz}$ denotes in-plane averaging of field g , namely $(L_x L_z)^{-1} \int_0^{L_z} \int_0^{L_x} g dx dz$. By averaging the z and x components of the vorticity equation $\nabla \times$ (A2b) we obtain

$$(a) \quad \frac{\partial}{\partial t} \frac{\partial^2 \phi_x}{\partial y^2} = \frac{\partial \langle \mathbf{N}_x \rangle_{xz}}{\partial y} + \frac{1}{\text{Re}} \frac{\partial^4 \phi_x}{\partial y^4}, \quad (b) \quad \frac{\partial}{\partial t} \frac{\partial^2 \phi_z}{\partial y^2} = \frac{\partial \langle \mathbf{N}_z \rangle_{xz}}{\partial y} + \frac{1}{\text{Re}} \frac{\partial^4 \phi_z}{\partial y^4}. \quad (A4)$$

Fields ϕ_x and ϕ_z are defined up to arbitrary functions of time that can be fixed as follows: The streamwise bulk velocity is given by the difference between the boundary values of ϕ_x at $y = \pm 1$, $U_m = \frac{1}{2} \int_{-1}^{+1} \langle u_x \rangle_{xz} dy = \frac{1}{2} [\phi_x(y, t)]_{y=-1}^{y=+1}$. The arbitrariness in the definition of ϕ_x can then be lifted by choosing $\phi_x(+1, t) = U_m(t)$; hence, $\phi_x(-1, t) = -U_m(t)$. Similar conditions apply to ϕ_z and W_m .

Equations for $U_m(t)$ and $W_m(t)$ are obtained by averaging (A2b) with respect to full space (x, y, z) :

$$(a) \quad \frac{dU_m}{dt} = \frac{1}{2\text{Re}} \left[\frac{\partial^2 \phi_x}{\partial y^2} \right]_{y=-1}^{y=+1} + \frac{2}{\text{Re}}, \quad (b) \quad \frac{dW_m}{dt} = \frac{1}{2\text{Re}} \left[\frac{\partial^2 \phi_z}{\partial y^2} \right]_{y=-1}^{y=+1}, \quad (A5)$$

where the term $2/\text{Re}$ in (A5a) accounts for the constant streamwise driving.

In addition to periodic boundary conditions applied at distances L_x and L_z to ω_y and u_y , the no-slip boundary conditions at the walls and the boundary conditions relative to ϕ_x and ϕ_z are

$$\begin{aligned} u_y|_{y=\pm 1} &= \left. \frac{\partial u_y}{\partial y} \right|_{y=\pm 1} = \omega_y|_{y=\pm 1} = \left. \frac{\partial \phi_x}{\partial y} \right|_{y=\pm 1} = \left. \frac{\partial \phi_z}{\partial y} \right|_{y=\pm 1} = 0, \\ \phi_x|_{y=\pm 1} &= \pm U_m, \quad \phi_z|_{y=\pm 1} = \pm W_m. \end{aligned} \quad (\text{A6})$$

The set of equations (A3)–(A5) with boundary conditions (A6) are numerically integrated as follows:

(a) Spatial treatment of (A3) uses Fourier series in streamwise and spanwise directions, x and z , respectively. In view of numerical accuracy and efficiency, the wall-normal dependence of (A3) is dealt with combinations of Chebyshev polynomials satisfying the homogeneous boundary conditions at $y = \pm 1$ [57]. The equations for ω_y and u_y are solved using the following expansions:

$$\omega_y = \sum_{l=0}^{L-2} \sum_{m=-M}^M \sum_{n=-N}^N \hat{\omega}^{lmn} [T_{l+2}(y) - T_l(y)] \exp \left[i \frac{2\pi}{L_x} mx + i \frac{2\pi}{L_z} nz \right], \quad (\text{A7})$$

$$u_y = \sum_{l=0}^{L-4} \sum_{m=-M}^M \sum_{n=-N}^N \hat{u}^{lmn} \left[T_{l+4}(y) - \frac{2l+4}{l+3} T_{l+2}(y) + \frac{l+1}{l+3} T_l(y) \right] \exp \left[i \frac{2\pi}{L_x} mx + i \frac{2\pi}{L_z} nz \right], \quad (\text{A8})$$

where T_l is the Chebyshev polynomial of degree l .

(b) Similarly, the auxiliary fields ϕ_x and ϕ_z in Eq. (A4) are expanded as

$$\phi_x = \sum_{l=0}^{L-4} \hat{\phi}_x^l \left[T_{l+4}(y) - \frac{2l+4}{l+3} T_{l+2}(y) + \frac{l+1}{l+3} T_l(y) \right] + \frac{U_m}{2} y(3-y^2), \quad (\text{A9})$$

$$\phi_z = \sum_{l=0}^{L-4} \hat{\phi}_z^l \left[T_{l+4}(y) - \frac{2l+4}{l+3} T_{l+2}(y) + \frac{l+1}{l+3} T_l(y) \right] + \frac{W_m}{2} y(3-y^2), \quad (\text{A10})$$

where the last terms in Eqs. (A9) and (A10) follow from the boundary-condition homogenization technique [58]; these terms are the polynomials of lowest degree satisfying all boundary conditions for ϕ_x and ϕ_z , respectively.

(c) A conventional Galerkin method is developed by taking the inner product of the basis functions and the evolution equations, yielding ordinary differential equations for each coefficient in the expansions. Periodic boundary conditions are imposed in the streamwise and spanwise directions at distances $L_x = 500$ and $L_z = 250$. Maximum Fourier wave numbers are $M = N = 767$ and the maximum degree for Chebyshev polynomials in the y direction is $L = 31$. Aliasing errors involved in the evaluation of the quadratic nonlinear terms are removed in all directions using the 2/3 rule [58] in the x and z directions and computing all coefficients of Chebyshev polynomials up to degree $2L$ in direction y . The evaluation of nonlinear terms then involves $(N_x, N_y, N_z) = (2304, 64, 2304)$ modes. For larger and smaller domain sizes $(L_x, L_z) = (1000, 500)$ and $(250, 125)$ used to check size effects, mode numbers are taken in the same proportions. This spatial resolution has been found appropriate from the comparison with other numerical simulations and a parallel study of plane Couette flow driven by countertranslating plates rather than by a constant body force. The equations are numerically time-integrated in a standard way using a second-order method, Crank-Nicolson for the viscous terms and Heun method for the other terms, with time increment $\delta t = 0.04$.

Other works may solve the flow using different definitions or scalings:

(a) In the literature, reference is often made to the mean flow rate. Here, the mean streamwise bulk velocity is a measured quantity that can characterize the flow regime upon time averaging; see Fig. 3(a) displaying $\langle U_m \rangle$ as a function of Re . From it, we can define a Reynolds number Re_b of practical use, though not a control parameter, as $\text{Re}_b = 1.5 \text{Re} \langle U_m \rangle$. Once our scaling is adopted for

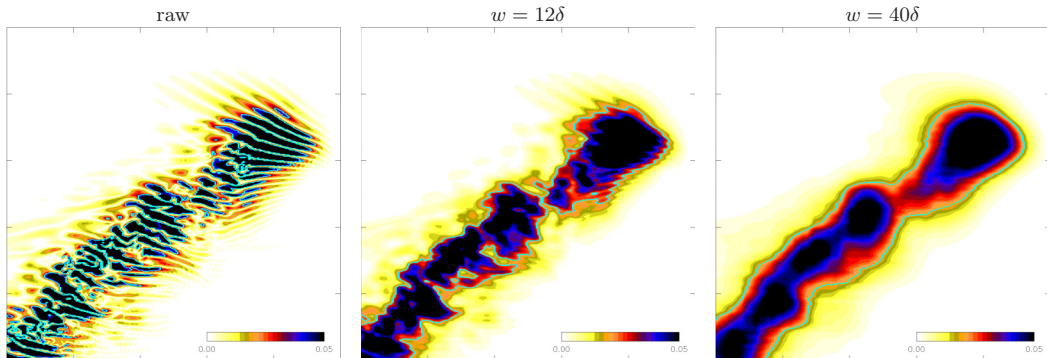


FIG. 11. Color-level illustration of the DAH of the LTB shown in Fig. 8 using $|u_y(x, 0, z)|$. The size of the domain displayed is $50 \times 50 \simeq 460\delta \times 460\delta$. Flow direction is from left to right. Raw data (left) and after box filtering with the width $w = 12\delta$ (routinely used here) and $w = 40\delta$. Light-blue lines mark the boundaries between turbulent and laminar regions as determined by the moment-preserving thresholding method.

the velocity, Re_b is then understood as the Reynolds number built using the center-plane velocity of a parabolic flow profile with the same mean velocity.

(b) Another popular choice is by using so-called *wall units*: The friction velocity is defined by $U_\tau^2 = \tau_w = \nu \langle |\partial_y u_x| \rangle_{\text{wall}}$. It is obtained by averaging (A2b) as $U_\tau^2 = 2/\text{Re}$ in our unit system; then,

$$\text{Re}_\tau = \text{Re} U_\tau = \sqrt{2\text{Re}}. \quad (\text{A11})$$

The friction coefficient is traditionally defined as $C_f = \tau_w / \frac{1}{2} \langle U_m \rangle^2$. In our approach, its expression directly comes from $\tau_w = U_\tau^2 = 2/\text{Re}$ to give $C_f = 4/(\text{Re} \langle U_m \rangle^2)$. Taking the inner product between \mathbf{u} and (2b) and averaging the equation then relates C_f to the mean dissipation rate $\langle \epsilon_m \rangle$. Expressed using $\langle U_m \rangle$ as the velocity unit, the volume-averaged dissipation rate $\epsilon_m(t) = 1.5(\text{Re}_b \langle U_m \rangle^2)^{-1} [\mathcal{V}^{-1} \int_{\mathcal{V}} (\nabla \mathbf{u} \cdot \nabla \mathbf{u}) d\mathcal{V}]$ is computed to give

$$\langle \epsilon_m \rangle = C_f / 2. \quad (\text{A12})$$

APPENDIX B: MEASUREMENT OF TURBULENT FRACTION

Local laminar and turbulent states are discriminated according to a traditional method of computer image treatment called “moment-preserving thresholding” [53]. The principle is to separate pixels in an image into several classes, using thresholds defined in a systematic way from the statistics of the pixels’ values, typically gray levels, rather than from some empirically defined rule. On general grounds, the thresholds are chosen so that the first few moments of the histograms of pixel values are preserved. In the present case, two classes distinguished through a single threshold, are needed: “turbulent \equiv above” and “laminar \equiv below.” Normalized histograms are obtained from the distribution of the observable, here simply called u , at all points in the domain, say $p(u)$. Its moments $m_k = \sum_u u^k p(u)$, $k = 1, 2, \dots$ are next computed. Unknown reduced variables \tilde{u}_ℓ with probability p_ℓ for laminar local states and \tilde{u}_t with probability $p_t = 1 - p_\ell$ for turbulent ones are then determined using three equations for the three lowest order moments [53]: $\tilde{u}_\ell^k p_\ell + \tilde{u}_t^k p_t = m_k$, $k = \{1, 2, 3\}$. (Multilevel thresholding would require more moments and, if the set of pixels were to be divided into M classes; it is easily seen that $2M - 1$ moments would then be required.) The reduced representation $(\tilde{u}_\ell, \tilde{u}_t)$ is thus the best two-level representation of the original field, while probability p_t corresponds to our evaluation of the turbulent fraction F_t .

The observable u of interest is here the box-filtered value of $|u_y(x, 0, z)|$ and a single parameter remains, the width w of the squares $w \times w$ over which $|u_y(x, 0, z)|$ is averaged. In order to visualize the result of the procedure, the laminar/turbulent cutoff u_* has to be determined. This is done by

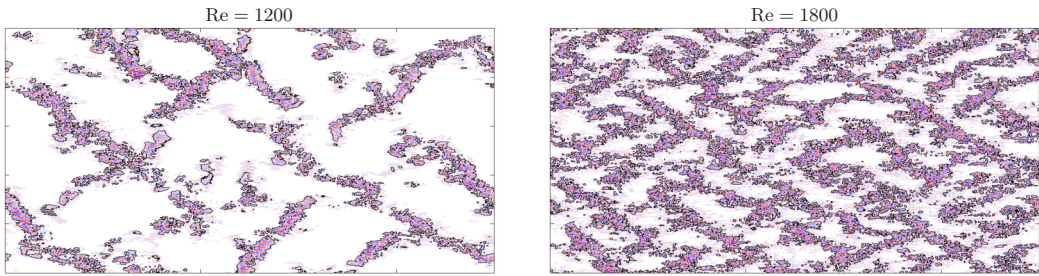


FIG. 12. Moment-preserving thresholding of snapshots at 1200 and 1800 in Figs. 1(c) and 1(d) under box filtering with $w = 12\delta$. Flow direction is from left to right. Domain size is 500×250 .

expressing the condition defining p_t explicitly, that is, $p_t = \#(u_i > u_*) / (N_x N_z)$, where $\#(u_i > u_*)$ is the number of lattice nodes considered as turbulent. The most faithful reproduction of the contour of turbulent domains requires that w should be large enough to damp out irrelevant small-scale modulations seen in Fig. 11, “raw.” The other panels in Fig. 11 illustrate the output of the procedure for different values of w . In the figure, δ stands for the spanwise grid spacing $\delta = L_z / N_z \simeq 0.109$. As the filter size becomes larger, spurious laminar regions disappear. A thin line corresponding to the cut-off condition $u = u_*$ delineates the turbulent region obtained with our thresholding method. Figure 12 displays the two snapshots in Fig. 1 belonging to the Re range studied in Sec. IV using $w = 12\delta$.

-
- [1] P. Huerre and M. Rossi, Hydrodynamic instabilities in open flows, in *Hydrodynamics and Nonlinear Instabilities*, edited by Claude Godrèche and Paul Manneville (Cambridge University Press, Cambridge, UK, 1998), pp. 81–294.
 - [2] P. J. Schmid and D. S. Henningson, *Stability and Transition in Shear Flows*, 2nd ed. (Springer, Berlin, 2012).
 - [3] S. A. Orszag, Accurate solution of the Orr-Sommerfeld stability equation, *J. Fluid Mech.* **50**, 689 (1971).
 - [4] J. Jiménez and P. Moin, The minimal flow unit in near-wall turbulence, *J. Fluid Mech.* **225**, 213 (1991).
 - [5] F. Waleffe, Exact coherent structures in channel flow, *J. Fluid Mech.* **435**, 93 (2001).
 - [6] G. Kawahara, M. Uhlmann, and L. van Veen, The significance of simple invariant solutions in turbulent flows, *Annu. Rev. Fluid Mech.* **44**, 203 (2012).
 - [7] S. Zammert and B. Eckhardt, Streamwise and doubly-localized periodic orbits in plane Poiseuille flow, *J. Fluid Mech.* **761**, 348 (2014).
 - [8] D. Coles, Transition in circular Couette flow, *J. Fluid Mech.* **21**, 385 (1965).
 - [9] C. D. Andereck, S. S. Liu, and H. L. Swinney, Flow regimes in a circular Couette flow system with independently rotating cylinders, *J. Fluid Mech.* **164**, 155 (1986).
 - [10] A. Prigent, G. Grégoire, H. Chaté, and O. Dauchot, Long-wavelength modulation of turbulent shear flows, *Phys. D (Amsterdam, Neth.)* **174**, 100 (2003).
 - [11] L. Tuckerman and D. Barkley, Patterns and dynamics in transitional plane Couette flow, *Phys. Fluids* **23**, 041301 (2011).
 - [12] E. Deusebio, G. Brethouwer, P. Schlatter, and E. Lindborg, A numerical study of the unstratified and stratified Ekman layer, *J. Fluid Mech.* **755**, 672 (2014).
 - [13] L. Klotz, G. Lemoult, I. Frontzák, L. S. Tuckerman, and J. E. Wesfreid, Couette-Poiseuille flow experiment with zero mean advection velocity: Subcritical transition to turbulence, *Phys. Rev. Fluids* **2**, 043904 (2017).
 - [14] E. Deusebio, C. P. Caulfield, and J. R. Taylor, The intermittency boundary in stratified plane Couette flow, *J. Fluid Mech.* **781**, 298 (2015).

- [15] S. Hashimoto, A. Hasobe, T. Tsukahara, Y. Kawaguchi, and H. Kawamura, An experimental study on turbulent-stripe structure in transitional channel flow, Sixth International Symposium on Turbulence, Heat and Mass Transfer, Rome, Sep. 14–18, 2009 (unpublished).
- [16] T. Tsukahara, Y. Seki, H. Kawamura, and D. Tochio, DNS of turbulent channel flow at very low Reynolds numbers, Fourth International Symposium on Turbulence and Shear Flow Phenomena, Williamsburg, June 27–29, 2005 (unpublished).
- [17] D. Barkley and L. Tuckerman, Computational Study of Turbulent Laminar Patterns in Couette Flow, *Phys. Rev. Lett.* **94**, 014502 (2005).
- [18] L. Tuckerman, T. Kreilos, H. Schrobdsdorff, T. M. Schneider, and J. F. Gibson, Turbulent-laminar patterns in plane Poiseuille flow, *Phys. Fluids* **26**, 114103 (2014).
- [19] B. Eckhardt, Turbulence transition in pipe flow: 125th anniversary of the publication of Reynolds’ paper—Introduction to the theme issue, *Philos. Trans. R. Soc. London A* **367**, 449 (2009).
- [20] K. Avila, D. Moxey, A. de Lozar, M. Avila, D. Barkley, and B. Hof, The onset of turbulence in pipe flow, *Science* **333**, 192 (2011).
- [21] N. Tillmark and P. H. Alfredsson, Experiments on transition in plane Couette flow, *J. Fluid Mech.* **235**, 89 (1992).
- [22] D. R. Carlson, S. E. Widnall, and M. F. Peeters, A flow-visualization study of transition in plane Poiseuille flow, *J. Fluid Mech.* **121**, 487 (1982).
- [23] G. Lemoult, J.-L. Aider, and J. E. Wesfreid, Turbulent spots in a channel: Large-scale flow and self-sustainability, *J. Fluid Mech.* **731**, R1 (2013).
- [24] K. Takeishi, G. Kawahara, H. Wakabayashi, M. Uhlmann, and A. Pinelli, Localized turbulence structures in transitional rectangular-duct flow, *J. Fluid Mech.* **782**, 368 (2015).
- [25] T. Ishida, Y. Duguet, and T. Tsukahara, Turbulent bifurcations in intermittent shear flows: From puffs to oblique stripes, *Phys. Rev. Fluids* **2**, 073902 (2017).
- [26] D. Barkley and L. Tuckerman, Mean flow of turbulent-laminar patterns in plane Couette flow, *J. Fluid Mech.* **576**, 109 (2007).
- [27] Y. Pomeau, Front motion, metastability and subcritical bifurcations in hydrodynamics, *Phys. D (Amsterdam, Neth.)* **23**, 3 (1986).
- [28] M. Henkel, H. Hinrichsen, and S. Lübeck, *Non-equilibrium Phase Transitions* (Springer, Berlin, 2008), Vol. 1.
- [29] D. Barkley, Simplifying the complexity of pipe flow, *Phys. Rev. E* **84**, 016309 (2011).
- [30] L. Shi, M. Avila, and B. Hof, Scale Invariance at the Onset of Turbulence in Couette Flow, *Phys. Rev. Lett.* **110**, 204502 (2013).
- [31] G. Lemoult, L. Shi, K. Avila, S. V. Jalikop, M. Avila, and B. Hof, Directed percolation phase transition to sustained turbulence in Couette flow, *Nat. Phys.* **12**, 254 (2016).
- [32] Y. Hiruta and S. Toh, Subcritical laminar-turbulence transition with wide domains in simple two-dimensional Navier-Stokes flow without walls, [arXiv:1805.04257](https://arxiv.org/abs/1805.04257) (unpublished).
- [33] M. Chantry, L. S. Tuckerman, and D. Barkley, Universal continuous transition to turbulence in a planar shear flow, *J. Fluid Mech.* **824**, R1 (2017).
- [34] M. Shimizu, G. Kawahara, and P. Manneville, Onset of sustained turbulence in plane Couette flow, Extended Abstracts of the Ninth JSME-KSME Thermal and Fluids Engineering Conference, Okinawa, Oct. 28–30, 2017 (unpublished).
- [35] M. Sano and K. Tamai, A universal transition to turbulence in channel flow, *Nat. Phys.* **12**, 249 (2016).
- [36] J. Tao and X. Xiong, The unified transition stages in linearly stable shear flows, Fourteenth Asia Congress of Fluid Mechanics, Hanoi and Halong, Oct. 15–19, 2013 (unpublished).
- [37] X. Xiong, J. Tao, S. Chen, and L. Brandt, Turbulent bands in plane-Poiseuille flow at moderate Reynolds numbers, *Phys. Fluids* **27**, 041702 (2015).
- [38] T. Tsukahara and T. Ishida, Lower bound of subcritical transition in plane Poiseuille flow, *Nagare* **34**, 383 (2015).
- [39] T. Kanazawa, M. Shimizu, and G. Kawahara, A two-dimensionally localized turbulence in plane channel flow, Extended Abstracts of the Ninth JSME-KSME Thermal and Fluids Engineering Conference, Okinawa, Oct. 28–30, 2017 (unpublished).

- [40] J. Tao, B. Eckhardt, and X. Xiong, Extended localized structures and the onset of turbulence in channel flow, *Phys. Rev. Fluids* **3**, 011902 (2018).
- [41] B. Hof, Transition to turbulence, Workshop on Extreme Events and Criticality in Fluid Mechanics: Computations and Analysis, The Fields Institute, Toronto, Jan. 25–29, 2016 (unpublished).
- [42] C. S. Paranjape, Y. Duguet, and B. Hof, Bifurcation scenario for turbulent stripes in plane Poiseuille flow, Sixteenth European Turbulence Conference, Stockholm, Aug. 21–24, 2017 (unpublished).
- [43] See Supplemental Material at <http://link.aps.org/supplemental/10.1103/PhysRevFluids.4.113903> for movies.
- [44] T. Teramura and S. Toh, Chaotic self-sustaining structure embedded in the turbulent-laminar interface, *Phys. Rev. E* **93**, 041101(R) (2016).
- [45] S. B. Pope, *Turbulent Flows* (Cambridge University Press, Cambridge, UK, 2000).
- [46] R. B. Dean, Reynolds number dependence of skin friction and other bulk flow variables in two-dimensional rectangular duct flow, *J. Fluids Eng.* **100**, 215 (1978).
- [47] V. C. Patel and M. R. Head, Some observations on skin friction and velocity profiles in fully developed pipe and channel flows, *J. Fluid Mech.* **38**, 181 (1969).
- [48] P. Manneville and M. Shimizu, Subcritical transition to turbulence in wall-bounded flows: The case of plane Poiseuille flow, in *22ème Rencontre du Non Linéaire* (2019), <http://nonlineaire.univ-lille1.fr/SNL/>.
- [49] M. Shimizu, P. Manneville, Y. Duguet, and G. Kawahara, Splitting of a turbulent puff in pipe flow, *Fluid Dyn. Res.* **46**, 061403 (2014).
- [50] P. Manneville, On the growth of laminar–turbulent patterns in plane Couette flow, *Fluid Dyn. Res.* **44**, 031412 (2012).
- [51] D. Barkley, Theoretical perspective on the route to turbulence in a pipe, *J. Fluid Mech.* **803**, P1 (2016).
- [52] H.-Y. Shih, T.-L. Hsieh, and N. Goldenfeld, Ecological collapse and the emergence of travelling waves at the onset of shear turbulence, *Nat. Phys.* **12**, 245 (2016).
- [53] W.-H. Tsai, Moment-preserving thresholding - A new approach, *Comp. Vision Graphics Image Proc.* **29**, 377 (1985).
- [54] The agreement is qualitative because the Barkley-Tuckerman oblique geometry [17] is only appropriate for bands generated by periodic continuation at a short distance along their own direction, which (i) reinforces coherence along that direction, (ii) forbids the opening of laminar gaps and the account of LTBs around Re_g , and (iii) kills orientation fluctuations and/or superpositions near Re_c , all together leading to an upward shift of the effective Reynolds number with regard to its nominal value.
- [55] Finite-size effects linked to this methodological difference presumably roots a systematic discrepancy between our definition of the mean-flow based Reynolds number and the one in Ref. [35], leaving us unable to match results about DP thresholds quantitatively.
- [56] M. Shimizu and P. Manneville, On the decay of localized turbulent bands in channel flow (unpublished).
- [57] J. Shen, Efficient spectral-Galerkin method II. Direct solvers of second- and fourth-order equations using Chebyshev polynomials, *SIAM J. Sci. Comp.* **16**, 74 (1995).
- [58] J. P. Boyd, *Chebyshev and Fourier Spectral Methods* (Dover Publications, New York, 2000).